JCTC Journal of Chemical Theory and Computation

Modeling the Morphology and Phase Stability of TiO$_2$ Nanocrystals in Water

A. S. Barnard,*,[†] P. Zapol,[†,‡] and L. A. Curtiss[‡]

Center for Nanoscale Materials and Materials Science and Chemistry Divisions, Argonne National Laboratory, 9700 South Cass Avenue, Argonne, Illinois 60439

Abstract: The potential of titanium dioxide nanoparticles for advanced photochemical applications has prompted a number of studies to analyze the size, phase, and morphology dependent properties. Previously we have used a thermodynamic model of nanoparticles as a function of size and shape to predict the phase stability of titanium dioxide nanoparticles, with particular attention given to the crossover of stability between the anatase and rutile phases. This work has now been extended to titanium dioxide nanoparticles in water, to examine the effects of various adsorption configurations on the equilibrium shape and the phase transition. Density functional calculations have been used to accurately determine surface energies and surface tension of low index hydrated stoichiometric surfaces of anatase and rutile, which are presented along with a brief outline of the surface structure. We have shown that morphology of TiO$_2$ nanocrystals is affected by the presence of water, resulting in variations in the size of the (001) and (00$\bar{1}$) truncation facets in anatase, and a reduction in the aspect ratio of rutile nanocrystals. Our results also highlight that the consideration of hydrated nanocrystal surfaces is necessary to accurately predict the correct size dependence of the anatase to rutile phase transition.

I. Introduction

Titanium dioxide (TiO$_2$) is an important accessory oxide mineral[1] used widely in science and technology.[2−5] Nanoparticles of this material are proving to be highly suitable for advanced photochemical applications,[6] especially interfacing with organic molecules[7] including DNA.[8] While the nanoscale dimension is instrumental in facilitating many new technologies, the size, phase, and morphology have been found to be critical parameters in determining their suitability for particular applications.[9−13]

Although macroscopically the rutile phase is more thermodynamically stable than the anatase phase[14] (at ambient pressures and temperatures), anatase has been found to be a majority product of industrial sol-gel, and aerosol syntheses of TiO$_2$,[3] and is common in nanoscale natural and synthetic samples.[5,15,16] Gribb and Banfield,[3] and later Zhang and

Banfield,[4] found that the synthesis of nanocrystalline TiO$_2$ consistently resulted in anatase nanoparticles, which transformed to rutile upon reaching a particular size (<14 nm). The transformation from anatase to rutile has been observed under different experimental conditions depending upon parameters such as temperature[17,18] and size. This implies that the transition energetics are closely coupled with the particle size[19] and that anatase is in fact the most stable polymorph at the nanoscale.

It has been proposed by a number of authors that the anatase to rutile phase transformation is not only dependent on grain size but also on impurities,[20−22] reaction atmosphere,[23,29] and synthesis conditions.[24−28] Yang et al.[27] showed that synthesis conditions (chemicals/peptizing agents) affect the crystallinity and phase transition temperature. In this vein, Zaban et al.[28] noted that the surface structure of TiO$_2$ is affected by the preparation conditions; and Ahonen et al.[29] observed that anatase synthesized in air transformed to rutile at 973 K, but anatase synthesized in nitrogen transformed to rutile at 1173 K. It has also been shown that nanocrystalline TiO$_2$ may be phase selected by careful control of

* Corresponding author e-mail: amanda.barnard@anl.gov.
† Center for Nanoscale Materials, Argonne National Laboratory.
‡ Materials Science and Chemistry Divisions, Argonne National Laboratory.

the particle size as well as other experimental conditions.[30−32] In addition to the control of the size of anatase nanocrystals, the shape may also be manipulated,[31,33,34] which may in turn enhance the adsorption properties of the nanocrystals by increasing the effective area of preferred surface facets.

We suggest that nanocrystal morphology is also a factor affecting the phase stability[40] as, contrary to numerous misconceptions, anatase nanoparticles are not necessarily spherical.[35] For example, high-resolution transmission electron microscopy (HRTEM) micrographs of Penn and Banfield[36] clearly show that the tetragonal bipyramidal morphology persists down to 3−5 nm in diameter. Similarly, the morphology of larger (∼20 nm) rutile nanocrystals can be discerned from the TEM images of Aruna et al.[37]

As part of an ongoing study, we have previously used a thermodynamic model[38] based on the free energy of (arbitrary) nanocrystals as a function of size and shape to determine the minimum energy morphology of anatase and rutile at the nanoscale and to examine the phase stability of faceted TiO_2 nanocrystals,[39] as a function of surface hydrogenation.[40] The model predicted that a bifrustum Wulff construction[42] for anatase nanocrystals, and a bitetragonal bipyramidal Wulff construction of rutile nanocrystals, which became more squat as the coverage of hydrogen was increased.

Further, the results of our study predict that (at low temperatures) the anatase to rutile phase transition size also depends on the surface hydrogenation. For clean surfaces (vacuum conditions) this phase transition is predicted to occur at an average diameter of approximately 9.3 nm for anatase nanocrystals.[39] This transition point slightly decreases to 8.9 nm when the surface bridging oxygens are H-terminated but increases significantly to 23.1 nm when both the bridging oxygens and undercoordinated titanium atoms of the surface trilayer are H-terminated.[40] As an extension of our previous work, the present study uses the same model to examine the relative phase stability of nanoscale anatase and rutile in water. This is considered to be of vital importance, since TiO_2 nanoparticles are often produced and stored in solution.

The model takes as input the geometry of the nanocrystal morphology, the surface free energy (γ), and the surface tension (σ). The surface tension has a small but important effect on the calculation of the anatase to rutile phase transition.[43] We have generated a consistent set of surface energy and surface tension values for water terminated stoichiometric low index (1 × 1) surfaces of both anatase and rutile, using ab initio methods. Both molecular and dissociative adsorption configurations have been considered, and the relative stability of each configuration has been compared with the results of other authors where possible.

II. Methodology

The surface structure and energetics of the low index surfaces of rutile and anatase were investigated by comparing highly accurate first principles calculations of the total energy of two-dimensional slabs with the corresponding three-dimensional bulk lattice structures. The slabs were generated by the addition of a 10 Å vacuum layer in the crystallographic plane of interest and then terminating the 'cleaved' surfaces

with either molecular or dissociative H_2O, in a complete monolayer ($\theta = 1$). Both the bulk and surface slabs were relaxed prior to calculation of the total energies.

The first principles calculations have been carried out using Density Functional Theory (DFT) within the Generalized-Gradient Approximation (GGA), with the exchange-correlation functional of Perdew and Wang (PW91).[44] This has been implemented via the Vienna Ab initio Simulation Package (VASP),[45,46] which spans reciprocal space with a plane-wave basis up to a kinetic energy cutoff of 270 eV. We have used the Linear Tetrahedron Method (LTM) with a 4 × 4 × 4 Monkhorst-Pack k-point mesh, for both the initial relaxations of the TiO_2 slabs, and the final calculation of surface energies and surface tensions. Although this choice of k-mesh results in some superfluous k-points in the nonperiodic direction of the surface slabs, it was found that the inclusion of these k-points is more consistent with the LTM.

The electronic relaxation technique used here is an efficient matrix-diagonalization routine based on a sequential band-by-band residual minimization method of single-electron energies,[49,50] with direct inversion in the iterative subspace, whereas the ionic relaxation involves minimization of the Hellmann-Feynman forces. During the relaxations we have used ultrasoft, gradient-corrected Vanderbilt-type pseudopotentials (US−PP)[47,48] and real-space projected wave functions (to decrease the computational cost) and have relaxed to a convergence of 10^{-4} eV. The following (final) energy calculations were then performed using the Projected Augmented Wave (PAW) potentials,[51] with a basis set increased to a cutoff of 350 eV and reciprocal-space projected wave function (to improve accuracy), also to a convergence of 10^{-4} eV. PAW potentials are generally considered to be more accurate than the ultrasoft pseudopotentials,[52] since the radial cutoffs (core radii) are smaller than the radii used for the US pseudopotentials, and the fact that the PAW potentials reconstruct the exact valence wave function with all nodes in the core region (all electron).

III. TiO₂ Surface

The surface science of the titanium dioxide polymorphs has been investigated,[53] including numerous studies investigating the surface of H_2O-terminated stoichiometric anatase[54,56−58] and rutile.[57−60] However, as a consistent set of surface energies for both phases (calculated using the same theoretical technique and convergence criteria) is required to provide a suitable input for the phase stability model, we have undertaken our own calculations on the surfaces of interest. Thus, the surface free energy and surface tension have been determined for the structurally relaxed low index anatase and rutile surfaces.

The relaxed surface structures are also presented, for the purposes of comparison with other studies (where available) for the lowest energy adsorption geometries. This will be followed by the presentation of the calculated adsorption energies, surface energies, and surface tensions.

A. Anatase Surfaces. In the following description each atom in the outermost TiO_2 trilayer has been labeled (in Figure 1) according to species, with the subscript denoting the *atomic* layer with respect to the vacuum (layer (1) is the
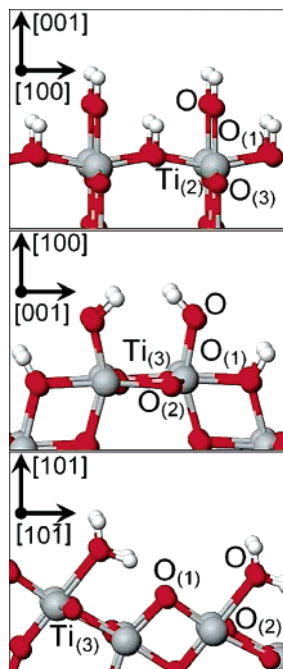
Figure 1. The relaxed anatase hydrated (001), (100), and (101) surfaces. The (001) and (100) surface exhibit dissociative adsorption, whereas the (101) surface exhibits molecular adsorption. The atoms occupying the atomic layers (denoted by the subscript) of the upper most trilayer labeled according to Table 1.

outermost layer of the surface TiO₂ trilayer). The oxygen associated with the adsorbate is denoted simply as O.

The hydrated surface trilayers of the anatase (001) surface are shown at the top of Figure 1. The clean surface contains 5-fold coordinated ($Ti_{(2)}$) atoms and 2-fold ($O_{(1)}$) and 3-fold coordinated ($O_{(3)}$) oxygens. Dissociative adsorption was found to be energetically favorable on this surface, with the H and OH terminations oriented perpendicular to the surface after relaxation. Compared with the clean surface,[39] the outward displacement of the oxygen atoms in the upper trilayer was found to decrease in the presence of water. This is most significant in the case of the $O_{(1)}$ bridging oxygen. In contrast the outward displacement of the $Ti_{(2)}$ was found to increase slightly in the presence of water. The final $Ti_{(2)}-$OH bond length was just under the equatorial Ti–O bond length of anatase, and the $O_{(1)}$–H bond length was found to be slightly longer than the O–H bond length in water (calculated to be 0.98 Å).

Calculated relaxations of these atoms are given in Table 1 along with the $O_{(1)}$–H and $Ti_{(2)}$–OH bond lengths. The displacement of selected atoms on the anatase (001) surface was examined by Bredow and Jug[58] using the semiempirical SINDO1 method and model clusters. The authors found that the bridging $O_{(1)}$ atoms relaxed outward by 0.12 Å, the $Ti_{(2)}$ atom relaxed outward by 0.16 Å, and the $Ti_{(2)}$–OH bond length was 1.85 Å, when a 4 × 4 × 3 cluster was used. Although the structure of the (001) surface was examined by Vittadini et al.,[54] they did not treat a complete monolayer of dissociatively adsorbed water. However, for a coverage of $\theta = 0.5$ (where the $O_{(1)}$–H terminations were removed) Vittadini et al.[54] reported $Ti_{(2)}$–OH bonds lengths between 1.74 and 1.93 Å.

Table 1: Comparison of Displacements (in Å), Normal to the Surface, of Atoms in the Uppermost Trilayer of the Hydrated and Clean[39] Anatase Surfaces, along with the Ti–OH₂ and O–H Bond Lengths

surface	label	clean[39]	hydrated
(001)	$O_{(1)}$	0.20	0.03
dissociative	$Ti_{(2)}$	0.04	0.09
	$O_{(3)}$	0.05	0.02
	Ti–OH		1.93
	$O_{(1)}$–H		1.01
(100)	$O_{(1)}$	0.18	−0.02
dissociative	$O_{(2)}$	0.04	0.01
	$Ti_{(3)}$	−0.16	0.10
	Ti–OH		1.87
	$O_{(1)}$–H		0.99
(101)	$O_{(1)}$	0.06	−0.01
molecular	$O_{(2)}$	0.28	0.10
	$Ti_{(3)}$	−0.12	−0.05
	Ti–OH₂		2.28

Like the (001) surface, the clean (100) surface contains 5-fold coordinated $Ti_{(3)}$ atoms and 2-fold $O_{(1)}$ and 3-fold coordinated $O_{(2)}$ atoms. When covered with a monolayer of dissociated water, the surface (shown in the center of Figure 1) was found to undergo an outward relaxation of the $O_{(2)}$ and $Ti_{(3)}$ atoms and a small inward relaxation of the $O_{(1)}$ atoms. The $Ti_{(3)}$–OH bond length was found to be 1.87 Å and the $O_{(1)}$–H bond length was 0.99 Å (see Table 1). The most interesting aspect of this surface was the bending of the O–H bonds of the OH groups toward each other, with a H–H distance of 2.6 Å.

The clean (101) surface contains 5-fold $Ti_{(3)}$ and 2-fold $O_{(1)}$ and 3-fold $O_{(2)}$ coordinated atoms within the first trilayer, with a characteristic saw-tooth profile perpendicular to the (010) direction. In this case molecular adsorption was found to be energetically preferred (see section 3.3) as indicated in the lower image of Figure 1. Following relaxation, both $O_{(1)}$ and $Ti_{(3)}$ atoms were found to contract inward, and the $O_{(2)}$ was found to relax outward (see Table 1). The $Ti_{(3)}-$OH₂ bond length of 2.28 Å matches the length of 2.28 Å reported by Vittadini et al.[54] for this bond.

The anatase (110) surface was found to be structurally unstable in the presence of water, both molecular and dissociated. The surface was found to deteriorate into a disordered structure. This structural change involved the breaking of symmetry as the 4-fold coordinated surface Ti atoms shifted from their lattice positions, and the desorption of OH and H₂O groups, sometimes involving $O_{(1)}$ atoms rather than the O atoms of the water molecules. Hence, the resulting surface could no longer be characterized as anatase, rendering it unsuitable for use in the phase stability model presented in the next section.

B. Rutile Surfaces. The (100), (110), and (011) surfaces are considered by applying the labeling convention used in the previous section for the anatase surfaces and are listed in Table 2. The corrugated (100) surface contains 5-fold coordinated $Ti_{(2)}$ atoms, with chains of 2-fold coordinated $O_{(1)}$ bridging atoms in the upper most atomic layer. This surface was found to prefer dissociative adsorption (as shown

Table 2: Comparison of Displacements (in Å), Normal to the Surface, of Atoms in the Uppermost Trilayer of the Hydrated and Clean[39] Rutile Surfaces, along with the Ti$-$OH$_2$ and O$-$H Bond Lengths

surface	label	clean[39]	hydrated
(100)	O$_{(1)}$	0.16	0.13
dissociative	Ti$_{(2)}$	0.06	0.02
	O$_{(3)}$	0.15	0.16
	Ti$-$OH		1.90
	O$_{(1)}-$H		0.99$-$1.01
	H-bonds (O$\cdots$H)		2.01$-$2.03
(011)	O$_{(1)}$	0.09	0.17
dissociative	Ti$_{(2)}$	0.05	0.19
	O$_{(3)}$	0.14	0.25
	Ti$-$OH		2.14$-$2.16
	O$_{(1)}-$H		1.01$-$1.08
	H-bonds (O$\cdots$H)		1.44$-$1.47
(110)	O$_{(1)}$	$-$0.19	0.08
molecular	Ti$_{(2)}$	0.40	0.35, $-$0.36
	O$_{(3)}$	0.24	$-$0.05
	Ti$-$OH$_2$		2.30
	H-bonds (O $\cdots$H)		1.66$-$1.67
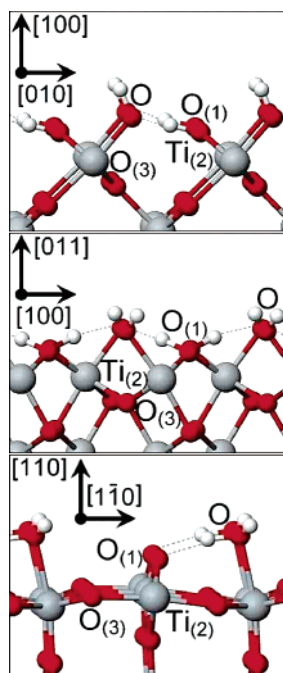
Figure 2. The relaxed rutile hydrated (100), (110), and (011) surfaces. The (100) and (011) surface exhibit dissociative adsorption, whereas the (110) surface exhibits molecular adsorption. The atoms occupying the atomic layers (denoted by the subscript) of the upper most trilayer labeled according to Table 2.

at the top of Figure 2), which is generally considered to be the case in other experimental and theoretical studies.[53] In general, the (outward) relaxation of the hydrated surface was found to be similar to the clean surface.[39] The Ti$_{(2)}-$OH bond length of 1.90 Å was found to be just under the equatorial Ti$-$O bond length of bulk rutile, and the O$_{(1)}-$H bond length was found to be just over the O$-$H bond length in water.

The hydrogen atoms terminating the bridging O$_{(1)}$ atoms were also found to form weak hydrogen bonds with the O

atoms of the OH groups, with an O$\cdots$H length of 2.01$-$2.03 Å. The issue of how well the PW91 exchange-correlation functional reproduces hydrogen bonding was briefly investigated by examining the relaxed geometry and binding energy of a water dimer and comparing with results obtained using second-order Møller$-$Plesset Perturbation theory (MP2) and the 6-311+G(3df,2p) basis set.[55] The PW91$-$PAW (MP2) optimized structure was found to have an O$-$O distance of 2.89 Å (2.90 Å) and an O$\cdots$H hydrogen bond length of 1.90 Å (1.94 Å), with a binding energy of 0.177 eV (0.234 eV). The good agreement between the PW91$-$PAW and MP2 results indicates that the method used here in the calculation of surface properties is capable of describing H-bonding reasonably well.

The (011) surface (center of Figure 2) has a ridged-like structure and was also found to prefer dissociative adsorption. The upper trilayer was found to relax outward approximately 0.1 Å more than the clean surface. The Ti$_{(2)}-$OH$_2$ bonds were longer than the rutile apical and equatorial Ti$-$O bond lengths. Similarly, the O$_{(1)}-$H bond lengths were considerably longer than the O$-$H bond in water. Like the (100) surface, hydrogen bonds were observed between the hydrogen atoms connected to the bridging oxygens and the oxygen atoms of the OH groups but with a considerably reduced length of 1.44$-$1.47 Å.

Finally, the relaxed hydrated (110) surface (see lower image of Figure 2), containing inequivalent Ti atoms lying in a centered rectangular arrangement, was found to prefer molecular adsorption. There is some disagreement in the literature as to whether water adsorbs on this surface molecularly or dissociatively, but in most cases experimental investigations indicate molecular adsorption.[53] Other theoretical studies have concluded that molecular adsorption is most probable,[61,62] and it has also been suggested that molecular and dissociative water may coexist on the rutile (110) surface.[59]

Even though our results indicate molecular adsorption, the structure of the surface is somewhat distorted by the presence of water, as shown in the lower image of Figure 2. On the clean surface, the Ti$_{(2)}$ atoms denoted as connected to the bridging oxygen (center of the image) are 6-fold coordinated, while the exposed Ti$_{(2)}$ atoms at the sides of the image are 5-fold coordinated. These Ti$_{(2)}$ atoms become inequivalent (see Table 2) on the hydrated surface, with the Ti$_{(2)}$ atoms bound to the bridging O$_{(1)}$ relaxing outward, and the Ti$_{(2)}$ atoms bound to the water molecules relaxing inward.

This layer distortion has been observed before[60,62] and is in part due to the accommodation of H-bonding between the bridging O$_{(1)}$ atoms and hydrogens in the water molecules. The length of these H-bonds of 1.66$-$1.67 Å is in good agreement with the result 1.6$-$1.8 Å calculated by Langel[62] using Car Parinello Molecular Dynamics (CPMD), and the value of 1.61 Å is calculated by Ferris and Wang using the self-consistent field (SCF) method and 3-21G basis set but is considerably less that the 2.22 Å calculated by Menetrey et al.[60] using PW91$-$USPP.

Like the anatase (110) surface, the rutile (001) surface was found to be unstable (with respect to a disordered surface structure) in the presence of water, exhibiting bond breaking

and symmetry breaking upon relaxation. This instability has (like the anatase (110) surface) been attributed to the 4-fold coordinated Ti atoms on the surface.

C. Surface Energetics. Although both molecular and dissociative adsorption geometries were examined on the surfaces described above, the previous section only outlines the details of the energetically preferred configuration. The distinction as to which geometry constituted the energetically preferred configuration was made by comparing the adsorption energies using the expression

$$E_{\text{ad}} = \frac{1}{N_{\text{H}_2\text{O}}}(E_{\text{H}_2\text{O}}^{\text{surface}} - E_{\text{clean}}^{\text{surface}} + N_{\text{H}_2\text{O}}E_{\text{H}_2\text{O}}) \tag{1}$$

where $N_{\text{H}_2\text{O}}$ is the total number of H₂O units on the surface, $E_{\text{clean}}^{\text{surface}}$ is the total energy of the relaxed surface without water, $E_{\text{H}_2\text{O}}$ is the total energy of a free water molecule, and $E_{\text{H}_2\text{O}}^{\text{surface}}$ is the total energy of the water covered surface. The adsorption energies for all surfaces are given in Table 3, along with the results of other authors for comparison.

The value of the surface free energy γ was calculated from the total energy of the bulk (E_N^{bulk}) and surface (E_N^{surface}) slabs using the expressions

$$\gamma = \frac{G}{A} \tag{2}$$

and

$$G = \frac{1}{2}(E_N^{\text{surface}} - E_N^{\text{bulk}} - N_{\text{H}_2\text{O}}\mu_{\text{H}_2\text{O}}) \tag{3}$$

where G is the free energy of the slab, A is the area of the surface, and N is the number of TiO₂ units in the (stoichiometric) cell. To account for the surface hydration, $\mu_{\text{H}_2\text{O}}$ is the chemical potential of water, calculated using[63]

$$\mu_{\text{H}_2\text{O}} = E_{\text{H}_2\text{O}} + \frac{h\nu}{2} + k_{\text{B}}T\left[\ln\left(\frac{PV}{k_{\text{B}}T}\right)\right] \tag{4}$$

where k_{B} is Boltzmann's constant, T, P, and ν are the temperature, pressure, and vibrational frequencies of water in the reservoir, and V is the quantum volume

$$V = \left(\frac{h^2}{2\pi m k_{\text{B}}T}\right)^{3/2} \tag{5}$$

Experimental values for ν were used,[64] and the chemical potential was calculated at ambient temperature and pressure (298.15 K and 101.33 kPa).

The value of the surface tension σ was obtained using the expression

$$\sigma = \frac{\partial G}{\partial A} \approx \frac{\Delta G}{\Delta A} \tag{6}$$

By applying a two-dimensional uniform dilation in the plane of the surface (including optimization of all internal parameters) and calculating the free energy G as shown in eq 3 for each area, the change in free energy (ΔG) was found for a set of area dilations (ΔA). After plotting these results an

Table 3: Comparison of the Adsorption Energy E_{ad} (eV) as Indicated in Eq 1, Compared with the Hartree−Fock (HF) Results of Fahmi and Minot,[57] the DFT GGA Results of Vittadini et al.,[54] the DFT GGA Results of Lindan et al.,[59] and the DFT GGA Results of Menetrey et al.[60]

	this study		reference 57		reference 54	
anatase	dissoc.	molec.	dissoc.	molec.	dissoc.	molec.
(001)	−0.45	0.23	−1.248	−0.682		
(100)	−0.29	−0.24				
(101)	−0.48	−0.56			−0.44	−0.72

	this study		reference 59		reference 60	
rutile	dissoc.	molec.	dissoc.	molec.	dissoc.	molec.
(100)	−0.57	unstable[a]				
(011)	−0.98	−0.43				
(110)	−0.27	−0.82	−0.91	−0.99	−1.14	−1.03

[a] Proton transfer was observed during relaxation, resulting in dissociative geometry, indicating that this configuration was unstable with respect to H⁺+OH⁻ dissociation.

Table 4: Comparison of Surface Free Energy γ and Surface Tension σ (in J/m²), for the Clean[39] Hydrated Low Index Surfaces of Anatase

		clean[39]		hydrated	
surface	adsorption	γ	σ	γ	σ
(001)	dissociative	0.51	2.07	1.55	−0.37
(100)	dissociative	0.39	0.60	1.13	−0.59
(101)	molecular	0.35	0.51	1.03	0.45

Table 5: Comparison of Surface Free Energy γ and Surface Tension σ (in J/m²), for the Clean[39] and Hydrated Low Index Surfaces of Rutile

		clean[39]		hydrated	
surface	adsorption	γ	σ	γ	σ
(100)	dissociative	0.60	0.95	1.57	0.61
(011)	dissociative	0.95	1.50	1.79	1.36
(110)	molecular	0.47	1.25	1.08	0.92

estimate of the surface tension was obtained from the slope. The results of these calculations are contained within Tables 4 and 5 for anatase and rutile, respectively.

The relative stability of the low index anatase surfaces may be discerned by comparing the values of γ listed in Table 4. The thermodynamic sequence (101) < (100) < (001) is the same for the clean and hydrated surfaces; however, the surface tension σ varies considerably. On the hydrated (001) and (100) surfaces σ is negative, indicating a tendency for this surface to expand (rather than contract). If present on the surface of a nanocrystal it would produce a tensile dilation in the direction of the surface normal, rather than a contraction. In general the surface tension of the anatase surface was found to decrease in the presence of water.

Previously we have obtained the order of (110) < (100) < (011) for the clean rutile surfaces,[39] and once again, this is the same for the hydrated surfaces. The σ of the rutile surfaces (like anatase) was found to decrease when termi-

nated by water, but in this case all tensions remained compressive.

IV. Phase Stability of Faceted TiO$_2$ Nanocrystals in Water

Previously we have shown that for a given nanoparticle of material x, the free energy may be expressed (to first order) as a sum of contributions from the particle bulk and surfaces,[38–41] such that

$$G_x^o = G_x^{bulk} + G_x^{surface} \qquad (7)$$

The free energy of formation of a nanocrystal G_x^o is defined in terms of the surface energy γ_{xi} for each surface i, weighted by the factors f_i, such that $\sum_i f_i = 1$.

Hence,

$$G_x^o = \Delta_f G_x^o + \frac{M}{\rho_x}(1 - e)[q\sum_i f_i \gamma_{xi}] \qquad (8)$$

where $\Delta_f G_x^o$ is the standard free energy of formation of the bulk (macroscopic) material, M is the molar mass, ρ_x is the density, and e is the volume dilation induced by the surface tension (which cannot be ignored at the nanoscale). In general, the surface-to-volume ratio q and the weighting factors f_i must be calculated explicitly for each shape and the facet therein. In this model the size dependence is introduced not only by the surface-to-volume ratio q but also by the reduction of e as the crystal grows larger. The shape dependence is also introduced by q as well as the weighted sums of the surface energies and the surface tensions, corresponding to the surfaces present in the particular morphology of interest.

In general, the volume dilation due to the surface tension may be approximated using the Laplace-Young equation[38] for the effective pressure

$$P_{\text{eff}} = \frac{2\sigma_x}{R} \qquad (9)$$

where R is the average radius of the particle, so that (with the compressibility $\beta = 1/B_0$)

$$e = \frac{2\beta\sigma_x}{R} \qquad (10)$$

The surface tension is approximated by summing over the (weighted) surface tension of the crystallographic surfaces present on the nanocrystal

$$\sigma_x = \sum_i f_i \sigma_{xi} \qquad (11)$$

where σ_{xi} is defined in eq 6 and listed in Tables 3 and 4 for $x =$ anatase ($\mathscr{A}$) and rutile ($\mathscr{R}$), respectively. The values of β for anatase and rutile were previously calculated[39] by fitting energy versus volume curves to the Vinet equation of state.[65] The resulting values for anatase of 190 GPa and rutile of 218 GPa were in good agreement with the experimental values of 179 GPa measured by Arlt et al.[66] and of 211 GPa measured by Gerward and Olsen,[67] respectively.

Previously it has been determined that the Laplace-Young description of the pressure is suitable in the case of faceted nanocrystals and that the edge and corner effects are limited over a diameter of approximately 2 nm.[38–40] Therefore, the surface energies and surface tensions for each surface facet i, along with the molar mass of TiO$_2$, the density of anatase and rutile ($\rho_{\mathscr{A}} = 3.893$ g/cm^3 and $\rho_{\mathscr{R}} = 4.249$ g/cm^3), and the standard free energies of formation[68] ($\Delta_f G_{\mathscr{A}}^o$ and $\Delta_f G_{\mathscr{R}}^o$) are all that is required to compare the phase stability of faceted TiO$_2$ nanocrystals over this size.

It is important to note that for the reasons mentioned above (and outlined in refs 38 and 39) this model is not applicable for small nanoparticles but rather to the 2 nm to submicron range. Therefore, for small nanoparticles less than 2 nm it is still preferable to examine each morphology explicitly by undertaking suitable calculations of isolated nanoparticles (e.g.: DFT or Tight Binding).

At large sizes, in the range of 75–100 nm, the free energy of the surfaces is less than 10^{-4} J/mol, making the energetics of the surface less significant and other bulk effects more significant. For example, in this size regime the macroscopic (bulk) strain is as important as the surface strain, and the entopic effects of the bulk will be as important as the surface entropy. The present model does include the bulk strain but does not explicitly include other macroscopic thermodynamic arguments. For this reason, it is best applied to particles in the range 2–100 nm.

All of the calculations in the present study have been performed at $T = 0$, so that G_x^o is equivalent to the enthalpy of formation. It has been shown by Zhang and Banfield[4] that the change in the surface free energies with temperature is of the order of 10^{-4} J/m^2, so it has been assumed here that variations in the equilibrium morphology of anatase and rutile nanocrystals due to temperature effects will be negligible.

A. Predicting Nanomorphology. The standard method for determining the equilibrium morphology of a material is to generate the Wulff construction[42] using the surface energies. However, as the Wulff construction does not take into account the effects of surface tension it is possible that the morphologies of nanocrystals may deviate from this shape. Using the model described above, we have investigated this possibility by optimizing the nanoparticle shape, as a function of size.

Beginning with the Wulff constructions as the initial case, the morphology of anatase and rutile nanocrystals were defined in terms of two independent length parameters **A** and **B**, as shown in Figures 3 and 4. In the case of anatase, this shape may vary depending upon the energetic relationship between {101} and {001} forms. In either case, the side of this bipyramidal form is denoted **A**. In nature, anatase crystals often exhibit a truncated bipyramid, or bifrustum, with square facets in the (001) and (00$\bar{1}$) planes (displayed as the interior solid in Figure 3). The side of this 'truncation' facet is denoted **B**. The degree of truncation may therefore be described by the size of **B** with respect to **A** (where $0 \leq$ **B** $\leq$ **A**).

The Wulff construction for rutile predicts a tetragonal prism bounded by {110} surfaces and terminated by a pair of tetragonal pyramids bounded by {011} surfaces (see

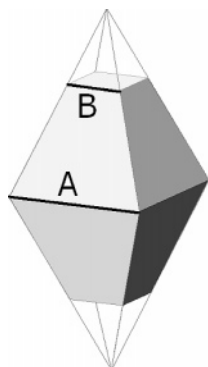TiO₂ Nanocrystals in Water

J. Chem. Theory Comput., Vol. 1, No. 1, 2005 **113**

Figure 3. An example of an anatase tetragonal {101} bipyramid is shown in outline, and an example of the bifrustum formed by addition of (001) and (00$\bar{1}$) truncation facets is shown as the interior solid. The side lengths labeled **A** and **B** are used to define the degree of truncation.
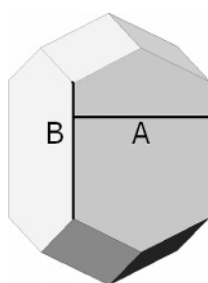

Figure 4. An example of the rutile tetragonal {110} prism terminated by a pair of tetragonal {011} pyramids. The side lengths labeled **A** and **B** are used to define the aspect ratio of the crystal.

Figure 4). The side of the tetragonal {110} prism is denoted **A**. In nature, the shape of rutile may vary from long acicular crystals to a short blocky habit. Therefore, the length of the tetragonal {110} prism is denoted **B**. The shape of the rutile crystal (the aspect ratio) may be described by the length of **B** with respect to **A** (where $0 \leq \mathbf{B} < \infty$).

By defining all the geometric parameters such as the volume and surface area of the various facets in terms of the ratio **B/A**, the energy was minimized with respect to this new variable. The numerical minimization was performed using a conjugate gradient scheme, in an attempt to find a value of **B/A** that produces a shape that is lower in energy than the Wulff construction as a function of size. This procedure was performed for 'clean' and hydrated anatase and rutile.

In the case of nanoscale anatase, shapes lower in energy than the Wulff construction were identified, as shown in Figure 5. Figure 5(a) shows a plot of the optimized **B/A** for sizes **A** = 2 to 300 nm, and Figure 5(b) shows the length of **B** for **A** in the same range. At very small sizes (in a vacuum and in water), the model predicts that small truncation facets of **B/A** = 0.32 and 0.30, even though the Wulff constructions (with same energies) predict values of **B/A** = 0.47 and 0.45. The size of these facets with respect to the overall size of the nanocrystal fluctuates somewhat, especially in the case of the clean surfaces for nanocrystals less than **A** = 100 nm. It is also important to note that as the model predicts that the size of the truncation facet will be slightly different
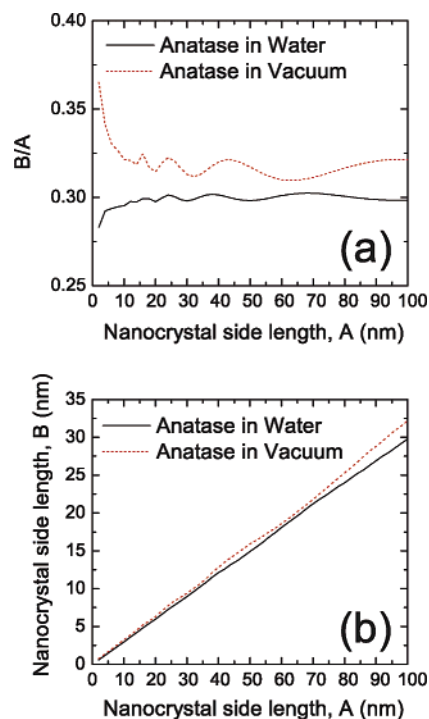

Figure 5. (a) Plot of the optimized ratio **B/A** and (b) length of **B** for each **A** for anatase nanocrystals in a vacuum and in water, with a side length **A** = 2 to 100 nm. The facet edges **A** and **B** are defined in Figure 3.

for clean and hydrated nanocrystals. In both cases, as the anatase crystals increase in size and the effects of surface tension diminish, the shape converges to that of the Wulff construction which remains the macroscopically lowest energy shape.

In the case of rutile, no lower energy shape was found, indicating that the Wulff construction dominates even at the nanoscale. It is important to note, however, that the optimization of rutile shape is more complicated than anatase since **B** has no upper bound. The length of **B** may therefore increase rapidly with respect to **A**, producing long needlelike crystals with a higher energy per TiO₂ unit than the Wulff construction. These nano-rod shaped crystals represent local minima in the shape-energy surface and are sampled due to the fact that the shape optimization described above acts only on the *open* form of the tetragonal {110} prism. During these optimizations the energy associated with the terminating tetragonal {011} pyramids remains constant.

The final shapes predicted by the model outlined above for anatase and rutile nanocrystals in a vacuum and in water (with a side length **A** ≤ 100 nm) are shown in Figure 6. These results predict that water reduces the (001) and (00$\bar{1}$) truncation facets at the apexes of the anatase nanocrystals and reduced the aspect ratio of the rutile nanocrystals.

B. Anatase to Rutile Phase Transition in Water. Finally, for each of the clean and hydrated nanocrystals shown in Figure 6, the value of $G^{\circ}_{\mathscr{A}}$ and $G^{\circ}_{\mathscr{R}}$ were calculated and plotted as a function of the number of TiO₂ units, by using the appropriate surface energies from Tables 4 and 5. In each case, the point of intersection of the free energies of anatase and rutile identifies the phase transition. These plots are shown
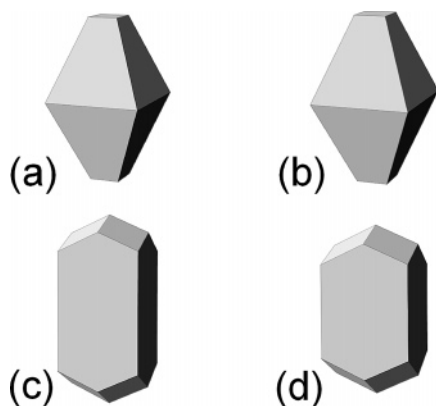
Figure 6. The morphology predicted in the present study for anatase (a) in a vacuum and (b) in water via optimization of the nanocrystal shape using the thermodynamic model described above and rutile (c) in a vacuum and (d) in water using the Wulff construction. These shapes correspond to nanocrystals with a side length (**A**) less than 100 nm.
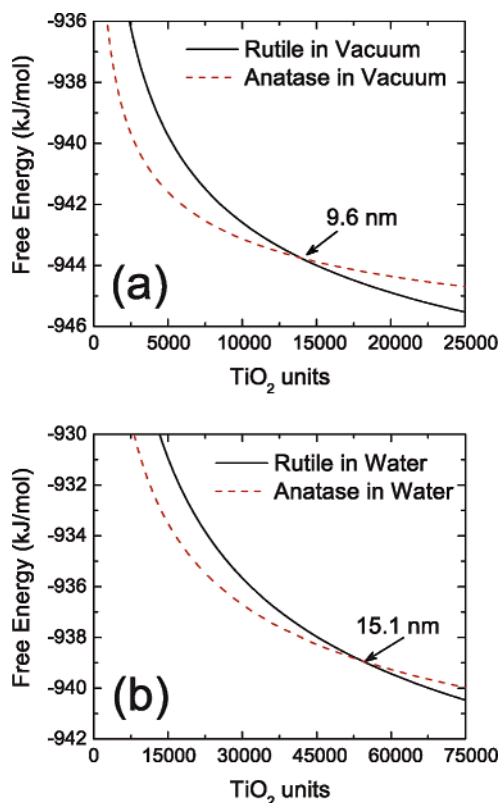

Figure 7. Free energy as a function of number of TiO_2 units for anatase and rutile (a) in a vacuum[39] and (b) in water, calculated using the shapes given in Figure 6 and the values of γ and σ from Tables 3 and 4. The intersection points indicate the phase transition.

in Figure 7 for nanoscale TiO_2 with (a) clean and (b) hydrated surfaces. The phase stability of TiO_2 in a vacuum has been reported before[39] and is included here for the purposes of comparison.

By comparing these results it is clear that the phase stability of nano-anatase is greater in water than in a vacuum. The intersection point for clean nanocrystals occurs at $\sim$12 600 TiO_2 units, corresponding to an anatase nanocrystal with average diameter of $\sim$9.6 nm. For nanocrystals in water

the intersection point occurs at $\sim$52 580 TiO_2 units, corresponding to an anatase nanocrystal with an average diameter of $\sim$15.1 nm. Experimentally, the transition point for hydrothermal samples at $\sim$650−800 K has been predicted to be at approximately 11.4−17.6 nm but has been found to decrease with temperature.[3]

Previously, a similar increase in the phase transition size of nano-anatase was predicted when the anatase and rutile surfaces were saturated with hydrogen.[40] At a full monolayer coverage of hydrogen the phase transition was predicted to be at $\sim$196 900 TiO_2 units, corresponding to an anatase nanocrystal with an average diameter of $\sim$23.1 nm. This is not the same as in water, indicating that it is not simply the termination of undercoordinated surface sites that affect the stability of nanoscale TiO_2, but also what these sites are terminated with. These striking results illustrate that the chemical environment plays an important part in phase stability and that the theoretical model used here is quite capable of describing these subtleties.

V. Conclusions

We have presented results of a thermodynamic model for the free energy of nanocrystals as a function of size and shape to illustrate the effects of water on the equilibrium shape and phase stability of anatase and rutile at the nanoscale. Using a complete set of values for the surface energy and surface tension of low index stoichiometric surfaces calculated using DFT GGA with the PAW potential method, we have shown that the morphology of TiO_2 nanocrystals is affected by the presence of water, resulting in variations in the size of the (001) and (00$\bar{1}$) truncation facets in anatase, and a reduction in the aspect ratio of rutile nanocrystals.

Our results for hydrated nanocrystals also predict (at low temperatures) an anatase to rutile phase transition size of $\sim$15.1 nm that is in good agreement with experiment,[3] highlighting that the consideration of appropriate surface passivation of nanocrystal surfaces is necessary to accurately predict the correct size dependence of the anatase to rutile phase transition. Further work is currently underway to examine the effects of pH on the phase transition size and shape.

References

(1) Banfield, J. F.; Bischoff, B. L.; Anderson, M. A. *Chem. Geol.* **1993**, *110*, 211−231.

(2) Elder, S. H.; Cot, F. M.; Su, Y.; Heald, S. M.; Tyryshkin, A. M.; Bowman, M. K.; Gao, Y.; Joly, A. G.; Balmer, M. L.; Kolwaite, A. C.; Magrini, K. A.; Blake, D. M. *J. Am. Chem. Soc.* **2000**, *122*, 5138−5146.

(3) Gribb, A. A.; Banfield, J. F. *Am. Mineral.* **1997**, *82*, 717−728.

(4) Zhang, H.; Banfield, J. F. *J. Mater. Chem.* **1998**, *8*, 2073−2076.

(5) Navrotsky, A.; Kleppa, O. J. *J. Am. Ceram. Soc.* **1967**, *50*, 626.

(6) Zhang, W. F.; Zhang, M. S.; Yin, Z.; Chen, Q. *Appl. Phys. B* **2000**, *70*, 261−265.

(7) Rajh, T.; Chen, L. X.; Lucas, L.; Liu, T.; Thurnauer, M. C.; Tiede, D. M. *J. Phys. Chem. B* **2002**, *106*, 10543−10552.

(8) Paunesku, T.; Rajh, T.; Wiederrecht, G.; Maser, J.; Vogt, S.; Stojićević, N.; Protić, M.; Lai, B.; Oryhon, J.; Thurnauer, M.; Woloschak, G. *Nature Mater.* **2003**, *2*, 343−346.

(9) Chen, L. C.; Rajh, T.; Jäger, W.; Nedeljkovic, J. M.; Thurnauer, M. C. *J. Synchrotron. Rad.* **1999**, *6*, 445−447.

(10) Rajh, T.; Nedeljkovic, J. M.; Chen, L. C.; Poluektov, O.; Thurnauer, M. C. *J. Phys. Chem. B* **1999**, *103*, 3515−3519.

(11) Zhang, H.; Penn, R. L.; Hamers, R. J.; Banfield, J. F. *J. Phys. Chem. B* **1999**, *103*, 4656−4662.

(12) Jang, K. D.; Kim, S.-K.; Kim, S.-J. *J. Nanoparticle Res.* **2001**, *3*, 141−147.

(13) Bullen, H.; Garrett, S. *Nano Lett.* **2002**, *2*, 739−745.

(14) Muscat, J.; Swamy, V.; Harrison, N. M. *Phys. Rev. B* **2002**, *65*, 224112.

(15) Mitsuhashi, T.; Kleppa, O. J. *J. Am. Ceram. Soc.* **1979**, *62*, 356.

(16) Zhang, H. Z.; Banfield, J. F. *J. Phys. Chem. B* **2000**, *104*, 3481−3487.

(17) Gourma, P. I.; Mills, M. J. *J. Am. Ceram. Soc.* **2001**, *84*, 619−622.

(18) Li, Y.; White, T.; Lim, S. H. *Rev. Adv. Mater. Sci.* **2003**, *5*, 211.

(19) Navrotsky, A. *Thermochemistry of Nanomaterials in Nanoparticles the Environment, Reviews in Mineralogy Geochemistry*; Banfield, J. F., Navrotsky, A., Eds.; Mineralog. Soc. Am.: 2001; Vol. 44.

(20) Arroyo, R.; Córdoba, G.; Padilla, J.; Lara, V. H. *Mater. Lett.* **2002**, *54*, 397−402.

(21) Arbiol, J.; Cerdà, J.; Dezanneau, G.; Cirera, A.; Peiró, F.; Cornet, A.; Morante, J. R. *J. Appl. Phys.* **2002**, *92*, 853−861.

(22) Francisco, M. S. P.; Mastelaro, V. R. *Chem. Mater.* **2002**, *14*, 2514−2518.

(23) Kittaka, S.; Matsuno K.; Takahara, S. *J. Solid State. Chem.* **1997**, *132*, 447−450.

(24) Zhang, H. Z.; Banfield, J. F. *J. Mater. Res.* **2000**, *15*, 437−448.

(25) Yoshinaka, M.; Hirota, K.; Yamaguchi, O. *J. Am. Ceram. Soc.* **1997**, *80*, 2749−2753.

(26) Okada, K.; Yamamoto, N.; Kameshima, Y.; Yasumori, A. *J. Am. Ceram. Soc.* **2001**, *84*, 1591−1596.

(27) Yang, J.; Mei, S.; Ferreira, J. M. F. *J. Am. Ceram. Soc.* **2000**, *83*, 1361−1368.

(28) Zaban, A.; Aruna, S. T.; Tirosh, S.; Gregg, B. A.; Mastai, Y. *J. Phys. Chem. B* **2000**, *104*, 4130−4133.

(29) Ahonen, P. P.; Kauppinen, E. I.; Joubert, J. C.; Deschanvres, J. L.; Van Tendeloo, G. *J. Mater. Res.* **2000**, *14*, 3938−3948.

(30) Zhang, H.; Finnegan, M.; Banfield, J. F. *Nano Lett.* **2001**, *1*, 81−85.

(31) Sugiyama, M.; Okazaki H.; Koda, S. *Jpn. J. Appl. Phys.* **2002**, *41*, 4666−4674.

(32) Sugimoto, T.; Zhou, X.; Muramatsu, A. *J. Colloidal. Int. Sci.* **2003**, *259*, 43−52.

(33) Sugimoto, T.; Okada, K.; Itoh, H. *J. Colloidal. Int. Sci.* **2003**, *193*, 140−143.

(34) Sugimoto, T.; Zhou, X.; Muramatsu, A. *J. Colloidal. Int. Sci.* **2003**, *259*, 53−61.

(35) Gao, Y.; Elder, S. A. *Mater. Lett.* **2000**, *44*, 228−232.

(36) Penn, R. L.; Banfield, J. F. *Geochim. Cosmochim. Acta* **1999**, *63*, 1549−1557.

(37) Aruna, S. T.; Tirosh S.; Zuban, A. *J. Mater. Chem.* **2000**, *10*, 2388.

(38) Barnard, A. S.; Zapol, P. *J. Chem. Phys.* **2004**, *121*, 4276−4283.

(39) Barnard, A. S.; Zapol, P. *Phys. Rev. B* **2004**, *70*, 235403.

(40) Barnard, A. S.; Zapol, P. *J. Phys. Chem. B* **2004**, *49*, 18435.

(41) Reference deleted in press.

(42) Wulff, G. *Z. Kristallogr. Mineral* **1901** *34*, 449.

(43) Lu, H. M.; Zhang, W. X.; Jiang, Q. *Adv. Eng. Mater.* **2003**, *5*, 787−788.

(44) Perdew, J.; Wang, Y. *Phys. Rev. B* **1992**, *45*, 13244.

(45) Kresse, G.; Hafner, J. *Phys. Rev. B* **1993**, *47*, RC558.

(46) Kresse, G.; Hafner, J. *Phys. Rev. B* **1996**, *54*, 11169.

(47) Kresse, G.; Furthmüller, J. *Comput. Mater. Sci.* **1996**, *6*, 15−50.

(48) Wood, D. M.; Zunger, A. *J. Phys. A* **1985**, *18*, 1343−1359.

(49) Vanderbilt, D. *Phys. Rev. B* **1990**, *41*, 7892.

(50) Kresse, G.; Hafner, J. *J. Phys.: Condens. Matter.* **1994**, *6*, 8245−8257.

(51) Blöchl, P. E. *Phys. Rev. B* **1994**, *50*, 17953.

(52) Kresse, G.; Joubert, D. *Phys. Rev. B* **1999**, *59*, 1758.

(53) Diebold, U. *Surf. Sci. Rep.* **2003**, *48*, 53−229.

(54) Vittadini, A.; Selloni, A.; Rotzinger, F. P.; Grätzel, M. *Phys. Rev. Lett.* **1998**, *81*, 2954.

(55) Redfern, P. C.; Zapol, P.; Curtiss, L. A.; Rajh, T.; Thurnauer, M. C. *J. Phys. Chem. B* **2003**, *107*, 11419−11427.

(56) Fahmi, A.; Minot, C. *Surf. Sci.* **1994**, *304*, 343−359.

(57) Bredow, T.; Jug, K. *Surf. Sci.* **1995**, *327*, 398−408.

(58) Lindan, P. J. D.; Harrison, N. M.; Gillian, M. J. *Phys. Rev. Lett.* **1998**, *80*, 762.

(59) Menetrey, M.; Markovits, A.; Minot, C. *Surf. Sci.* **2003**, *524*, 49−62.

(60) Redfern, P. C. **2004**, unpublished.

(61) Shapovalov, V.; Stefanovich, E. V.; Truong, T. N. *Surf. Sci. Lett.* **2002**, *498*, L103−L108.

(62) Langel, W. *Surf. Sci.* **2002**, *496*, 141−150.

(63) Rushbrook, G. S. *Introduction to Statistical Mechanics*; Clarendon Press: Oxford, 1957.

(64) *Handbook of Chemistry and Physics*, 84th ed.; Lide, D. R., Ed.; CRC Press: Boca Raton, 2003−2004.

(65) Vinet, P.; Rose, J. H.; Ferrante, J.; Smith, J. R. *J. Phys: Condens. Matter.* **1989**, *1*, 1941−1963.

(66) Arlt, T.; Bermejo, M.; Blanco, M. A.; Gerward, L.; Jiang, J. Z.; Staun Olsen, J.; Recio, J. M. *Phys. Rev. B* **2000**, *61*, 14414.

(67) Gerward, L.; Olsen, J. S. *J. Appl. Crystallogr.* **1997**, *30*, 259−264.

(68) The experimental free energies of formation of anatase (rutile) $\Delta_f G^o{}_{\mathscr{A}}$ ($\Delta_f G^o{}_{\mathscr{R}}$) taken from the JANAF tables have been applied here, such that $\Delta_f G^o{}_{\mathscr{A}} = -9.491471 \times 10^{-2}$ mJ/mol ($\Delta_f G^o{}_{\mathscr{R}} = -9.539962 \times 10^{-2}$ mJ/mol). Chase, M. W.; Davies, C. A.; Downey, J. R.; Frurip, D. J.; McDonald, R. A.; Syverud, A. N. *J. Phys. Chem. Ref. Data* **1985**, *14* (Suppl. 1), 1680.